TRANSITION INVESTIGATIONS ON A M=5 RAMP

Christian Stemmer
Lehrstuhl für Aerodynamik,
Technische Universität München
Boltzmannstr. 15, D-85748 Garching, Germany
christian.stemmer@tum.de

Nikolaus A. Adams
Lehrstuhl für Aerodynamik,
Technische Universität München
Boltzmannstr. 15, D-85748 Garching, Germany
nikolaus.adams@tum.de

ABSTRACT

Direct Numerical Simulations (DNS) have been used to investigate transitional shock wave/boundary-layer interaction for high-speed ramp flow at M=5 and a ramp angle of $\beta = 15°$.

The flow separates very early from the flat plate ahead of the ramp in a laminar environment. The flow within the separation bubble is complex as the reverse flow down the ramp separates as well and enables for positive velocities below the separated reverse flow. The reverse flow meanders and 'hits' the high-shear layer from below. This is the cause for weak oblique shock waves (shocklets) emanating from the upper surface of the high-shear layer into the free stream. This flow topology is very stable to boundary-layer instabilities. The most unstable first and second-mode instabilities for the unseparated case have been introduced at the inflow boundary. They reach moderate amplitudes ($1\% > u' > 10\%$) and lead to turbulent reattachment of the shear layer. The nature of the separation bubble is nevertheless not affected by the instabilities. The separation bubble moves with a frequency not associated with the disturbance frequencies. The reattachment line is distorted in spanwise direction through a longitudinal vortex.

INTRODUCTION

Transitional shock wave/boundary-layer interaction for high-speed flows is extremely important for the design of next-generation space-traveling vehicles and high-speed transport aircraft. Local laminar to turbulent breakdown of the boundary-layer flow can lead to peak heat loads on the structure with the possibility of failure. The generic geometry of a ramp is chosen generalizing the features present at possible air intakes or at joints of components. The shock/boundary-layer interaction is of particular interest (Pagella *et al.*, 2002, 2004, Lawal and Sandham, 2001) involving complex interactions of several instability mechanisms.

The present case was chosen as a RTO reference case for validation (Knight, 2003) and has been investigated experimentally (Vandomme, 2004, and Benay *et al.*, 2006) with varying disturbance backgrounds and stagnation pressure settings. One stagnation-pressure case is directly comparable with the current investigations ($p_{st} = 5 \cdot 10^5$Pa). Unfortunately, the geometry was changed from the original design, which is one of the reason why the numerical results presented here cannot be compared directly with the mentioned experimental works.

Turbulent simulations (Lüdeke *et al.*, 2004) suggest the presence of pairwise counter-rotating vortices in the reverse flow of the separation zone and near reattachment. Investigations for turbulent interactions for M=2.95 by Loginov *et al.*, 2006 by means of LES reveal Görtler-type vortices and details on complex shock wave/boundary-layer interaction.

General research on compressible boundary-layer transition was intense and numerous in the past years revealing many interesting features in flat-plate boundary layers as well as compression ramp configurations. Experimental results for compression corner boundary layer flows (some in comparison to numerical results) can be found in Stetson and Kimmel, 1992, and Bleilebens *et al.*, 2005, and for hypersonic cases including non-equilibrium effects in Wadhams and Holden, 2004. The separation in the corner was noticed for various conditions and Mach numbers, but the separating shear layer was straight and steady not showing any undulating behaviour of the reverse flow.

The dimensions for the current simulation were adapted to a case put forth in the Stage 1 Report of the RTO Working Group 10 on "Technologies for Propelled Hypersonic Flight", Subgroup 3 "CFD Validation for Hypersonic Flight", Version Jan. 7, 2000, data set number 2, heated hollow cylinder flare, by B. Chanetz and J. P. Davis. In the most up-to-date version of this report (Knight, 2003), this data set was omitted.

Vandomme, 2004 and Benay *et al.*, 2005 have followed a similar path in the experimental setup choosing a hollow cylinder flare. The diameter is large enough to compare the results qualitatively with the present flat-plate boundary layer. In the experiments, the length of the leading cylinder is smaller compared to the numerical setup by 20%. The experiments deviate from the simulation in a further point as the wall temperature at the beginning of the experiment was set to $T_W = 290K$ and rose over the course of the experiment to deduce the heat flux measurement as the time derivative of the temperature on the surface. Therefore, comparability is limited for this experiment. The turbulence level in the free stream was measured to $Tu \approx 2\%$ in Vandomme, 2004 and therefore, the length of the separation bubble is much smaller in the experiment. Among variations in stagnation pressure, Benay *et al.*, 2005 have compared their results for natural transition with the results from experiments where the transition was triggered

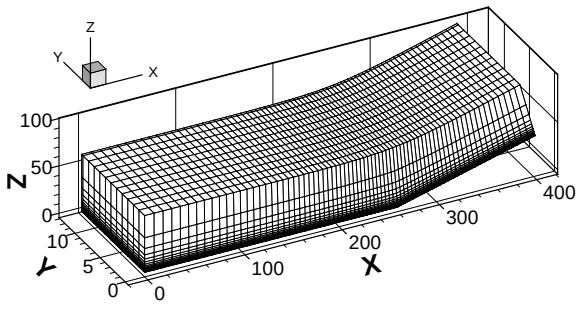

Figure 1: Computational grid, every tenth grid line shown – note the clustering close to the wall

by a circumferential surface roughness at $x/L = 0.08$ with a height of h=0.7mm. The flow became turbulent suppressing the separation bubble in the case of triggered transition. The case with a stagnation pressure of $p_{st} = 5 \cdot 10^5 Pa$ corresponds to the presented simulations.

GOVERNING EQUATIONS AND METHODOLOGY

Governing Equations

The fundamental equations solved are the conservative equations for mass, momentum and energy (three-dimensional, unsteady Navier-Stokes equations) in generalized coordinates

$$\frac{\partial U}{\partial t}+\frac{\partial}{\partial \xi}\frac{F_E}{J}+\frac{\partial}{\partial \eta}\frac{G_E}{J}+\frac{\partial}{\partial \zeta}\frac{H_E}{J}=\frac{\partial}{\partial \xi}\frac{F_S}{J}+\frac{\partial}{\partial \eta}\frac{G_S}{J}+\frac{\partial}{\partial \zeta}\frac{H_S}{J}. \quad (1)$$

The flux terms with the index E and S are numerically treated differently with finite differences of fifth and sixth order accuracy (Adams, 1998). The conservative variables are $\mathrm{U} = \{\rho, \rho u, \rho v, \rho w, E\}$. The energy is defined as $\mathrm{E} = p/(\gamma-1) + \rho/2(u^2+v^2+w^2)$. The generalized coordinates are only applied in the downstream (x) and the wall-normal (z) direction whereas the essentially two-dimensional configuration allows for equidistant spacing in spanwise (y) direction. The physical space $\{x, y, z\}$ is mapped onto the equidistant computational space $\{\xi, \eta, \zeta\}$. The details of the mapping and the definition of the convective and diffusive fluxes can be found in Adams, 1998. All variables are non-dimensionalized according to $x = x^*/\delta_1, u = u^*/U_\infty, \rho = \rho^*/\rho_\infty$, $T = T^*/T_\infty, E = E^*/(\rho U_\infty^2)$, where the * denotes dimensional quantities. The subscript $_\infty$ denotes the free-stream condition. Values with a prime ($'$) denote the disturbance quantities of the respective variable.

Numerical Method and Flow Parameters

A well-established sixth-order accurate numerical method (Adams and Shariff, 1996, Adams, 1998) is used. Compact finite differences are employed. Periodic conditions in the spanwise direction are enforced. A third-order accurate Runge-Kutta method is used for time advancement. The shock is treated by switching locally to an ENO method. For the presented simulation, a resolution of $3000 \times 180 \times 90$ points in streamwise (x), wall-normal (y) and spanwise (z) directions was used ($\sim$ 50 Mio points). The grid is stretched in the wall-normal and downstream directions allowing for the clustering of points around the corner and close to the wall as shown for every tenth grid point in Fig.1.

Table 1: Disturbance modes

Parameter	First mode	Second mode
α_r	0.4828	2.2061
α_i	-0.0064	-0.0123
β	1	0
ω	0.4	2
c_{phas}	0.83	0.91
(h,k)	(2,2)	(10,0)

All lengths have been non-dimensionalized by the boundary-layer thickness at inflow $\delta_1 = 0.2197$m. The ramp angle is $\beta = 15°$ and the free-stream Mach-number is 5. The inflow is started with a laminar boundary as a result form a boundary-layer calculation for a distance of $x_0^* = 2.53 \cdot 10^{-2} m$ from the leading edge, which is not part of the integration domain. The free-stream temperature is $T_0^* = 83.33K$ with an isothermal wall-temperature of $T_W^* = 4.8T_0^* = 400K$. The free-stream pressure is $p_0^* = 945Pa$ and the resulting free-stream velocity amounts to $U_0^* = 915\frac{m}{s}$.

RESULTS

First, a number of two-dimensional study was undertaken to attain a steady result for the developing separation bubble. The present resolution (3000x180 points) gave grid-independent results. A further increase in grid resolution to 5000x320 points in downstream and wall-normal direction respectively was used to confirm this (see Adams (2001) for details).

The most unstable first and second mode instability waves were taken as a reasonable guess for the disturbance inflow at the upstream boundary at a level of $u'/U_\infty = 10^{-4}$. The spatial development of the disturbed waves and nonlinearly generated waves is shown in Fig. 2, where the notation (h,k) denotes a wave with multiples h of the dimensionless fundamental frequency $\omega_0 = 0.2$ in time and k denotes multiples of the fundamental dimensionless spanwise wave number $\beta_0 = 0.5$ (the wave angle of the three-dimensional disturbance with $k = 2$ is 60°). For the parameters of the disturbances, see Table 1. The three-dimensional disturbance (2,2) is first amplified to a level of $u'/U_\infty \approx 2 \cdot 10^{-3}$. Due to the separation bubble, the disturbance waves are not amplified as postulated by the compressible stability theory (Mack, 1969) for supersonic boundary layer. Upstream of the ramp, the non-parallel effects stabilize the three-dimensional first-mode disturbance. The two-dimensional second-mode disturbance (10,0) is damped initially to reach its initial disturbance level only just before the ramp. The two disturbances do not lead to the laminar-turbulent breakdown as they would in the absence of the ramp (i.e. in the pure boundary layer). The largest amplitude steady mode is the mode (0,2) which exhibits comparable amplitudes to the unsteady disturbance amplitudes. All other steady modes exhibit a somewhat smaller amplitude indicating that the separation bubble is moving with a frequency not at all associated with the analyzing fundamental frequency (amplitudes are gained from a Fourier analysis in time over one period of the fundamental frequency - the maximum of the wall-normal profile is shown in the amplitude figure 2). Nonlinearly generated modes are not playing a significant role in the disturbance amplitude development upstream of the ramp indicating the laminar nature of the problem for such a low-level disturbance background. The disturbed first-mode instability (2,2) and the second-mode instability (10,0) are

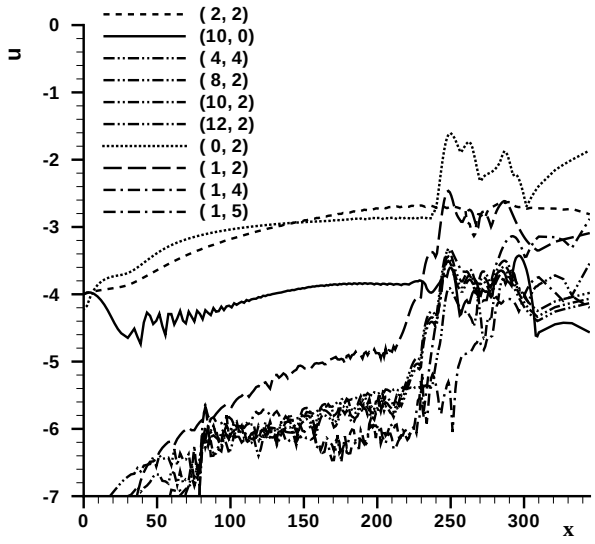

Figure 2: Amplitude of the downstream disturbance velocity u' – disturbance modes, nonlinear combinations thereof and selected other modes

not amplified enough to initiate the laminar-turbulent breakdown of the flow at the ramp.

At the location of the kink ($x = 260$), the amplitudes of all disturbance modes increase by one to two orders of magnitude. This leads to turbulent reattachment.

A numerical Schlieren Image (Fig. 3) has been produced with the help of the spanwise integration of the density gradient (with the number of point in spanwise direction npy)

$$\nabla\rho = \frac{1}{npy}\sum_{1}^{npy}\sqrt{\left(\frac{\partial\rho}{\partial x}\right)^2+\left(\frac{\partial\rho}{\partial y}\right)^2+\left(\frac{\partial\rho}{\partial z}\right)^2}. \qquad (2)$$

The shock emanating from the onset of separation ($x = 39$) extends towards the upper boundary of the integration domain without ever leaving the integration domain. The strong shear layer is also clearly visible and is reattaching at the ramp at $x = 372$. The shock emanating from the point of reattachment is also clearly distinguishable at $x \approx 380$. In the vicinity of the kink of the ramp (lower graph in Fig. 3), shocklets are generated in the shear layer at $x \approx 230 - 300$ emanating obliquely upwards satisfying the oblique shock conditions for the local Mach number. The source of the shocklets is located underneath the shear layer, where an undulating structure can be identified in the Schlieren image.

The spanwise integration of the pressure gradient shows the shocks but not the shear layer (Fig. 4) as expected. (The gradient of the density shows the shear layer very clearly.) The roller-like structures underneath the shear layer representing strong pressure gradients where the origin of the shocklets can be identified underline the acoustic origin of the shocklets. The shock emanating from the onset of separation is also present in the pressure gradient.

The total pressure in the vicinity of the kink is shown is Fig.5. The shocklets on top of the shear layer are rooted at locations where the pressure gradient is maximum underneath the shear layer. An almost constant negative pressure gradient can be identified along the ramp (the point of reattachment is outside the detailed representations at $x = 372$).

The total downstream instantaneous velocity U as shown in figure 6 reveals that the reverse flow underneath the shear

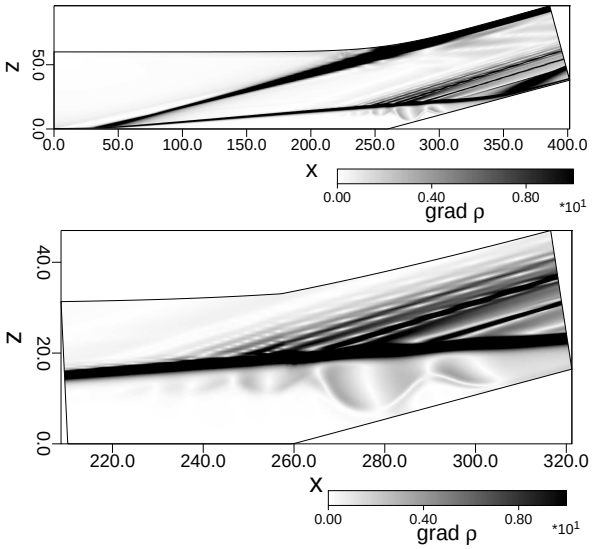

Figure 3: Numerical Schlieren image – integration of the gradient of the density ρ in spanwise direction – entire domain (upper graph) and details in the vicinity of the kink (lower graph)

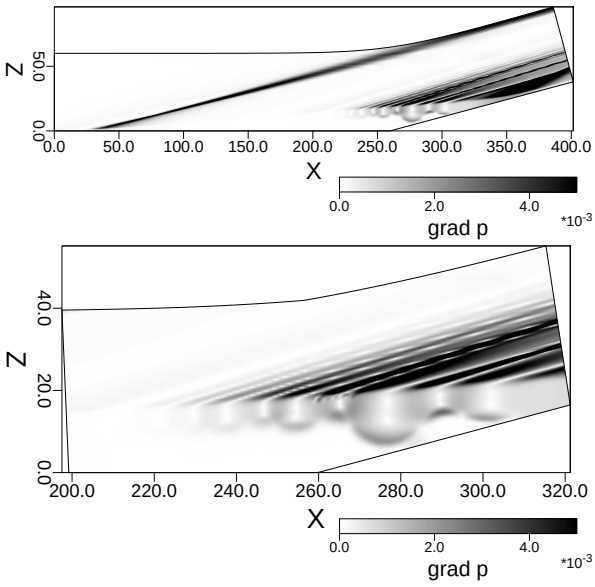

Figure 4: Integration of the gradient of the pressure p in spanwise direction – entire domain (upper graph) and details in the vicinity of the kink (lower graph)

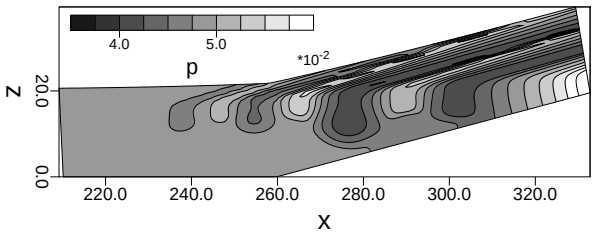

Figure 5: Pressure p in the vicinity of the kink

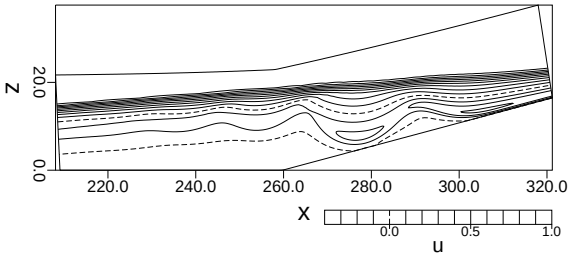

Figure 6: instantaneous total downstream velocity U as contours with the zero velocity level as a dashed line. Lines within the two dashed lines are negative values.

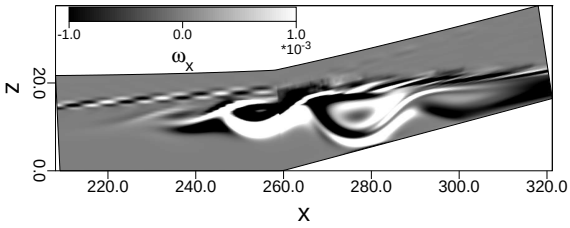

Figure 7: instantaneous downstream vorticity ω_x in a slice at about $\Delta z = L_z/4$ – the reference direction is always parallel to the wall

layer detaches from the wall with regions of upstream positive velocity closer to the wall. Conventional detachment criteria for wall-jets can not be applied to this case, since they postulate a free flow in the far field or an external pressure gradient. With the high-shear layer on top of the reverse flow, we believe that these criteria are inappropriate for this case. It can be stated that the adverse pressure gradient in the direction along the ramp where the separation of the reverse flow occurs is $\Delta p/\Delta l = -1200Pa/0.028m \approx -42857Pa/m$.

The shocklets that obliquely emanate upwards from the surface of the high-shear layer are triggered by the detached reverse flow. the meandering back flow 'bumps' against the shear layer from below. Together withthe pressure distribution underneath the shear layer, this causes the shocklets to occur.

Additional insight into the complex flow in proximity to the ramp is shown in the following figures 7 to 9. The streamwise vorticity ω_x is shown in figure 7 in a slice at about $\Delta z = L_z/4$. The oncoming disturbance is seen in the region of the shear layer (the shear layer itself does not show in ω_x). The vortex system as a result from the detached reverse flow in the kink region is clearly to be distinguished. The vortices are present twice along the spanwise extent of the integration domain. The spanwise vorticity (Fig. 8) is not affected by the initial disturbances and is also constant for all spanwise positions clearly showing the path of the reverse flow. the wall-normal vorticity (Fig. 9) basically shows the the same qualitative picture as the downstream vorticity.

The reattachment line (at about $x = 372$ in Fig. 10) is distorted in the spanwise direction due to the relatively large amplitude of the steady disturbance mode (0,2) which is due to the vortex system underneath the shear layer. As one follows the reverse flow on its way upstream ($x = 302 \sim 370$), the detachment of the reverse flow from the wall can be observed and a 'secondary bubble' at $x = 281 \sim 302$ and another one at $x = 177 \sim 275$ lies underneath the

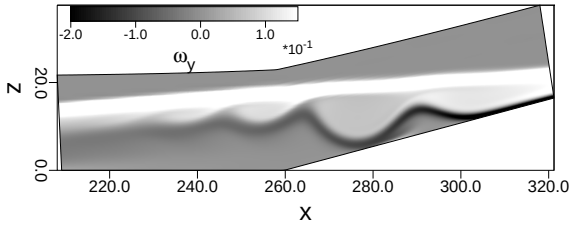

Figure 8: instantaneous spanwise vorticity ω_y in a slice at about $\Delta z = L_z/4$

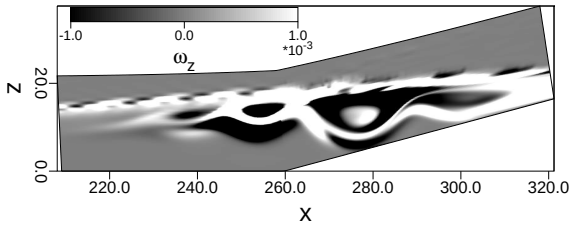

Figure 9: instantaneous wall-normal vorticity ω_z in a slice at about $\Delta z = L_z/4$ – the reference direction is always normal to the wall

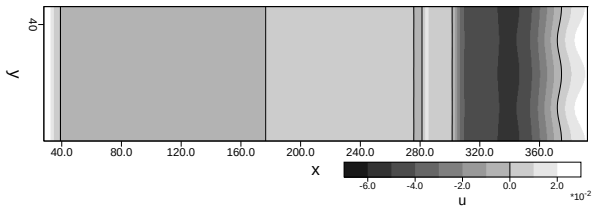

Figure 10: Downstream velocity u at the point next to the wall. The beginning of the ramp is at $x = 260$. Through the up and down of the reverse flow, an alternating two-dimensional pattern of reverse and downstream flow can be seen. At the reattachment point $x = 372$, the persistent steady mode (0,1) warps the reattachment line

band of reverse flow that impinges on the surface shortly at $x = 275 \sim 281$. The separation bubble has a very strong two-dimensional nature until it comes close to the point of reattachment. The up and down motion of the reverse flow is also a two-dimensional phenomenon.

CONCLUSIONS

The detailed structure of the flow along a 15° ramp at M=5 is presented. The separation bubble has a large streamwise extent. The shear layer and the underlying system of vortices and complex reverse flow path is presented. The reverse flow under the shear layer detaches from the upward part of the ramp leaving positive shear stress at the wall. The detached reverse flow hits the shear layer from below several times. These locations are the locations from where oblique compression waves (shocklets) originate.

The entire system is very stable with respect to the oncoming first and second-mode disturbances introduced at the inflow boundary at a level of $u'/U_\infty = 10^{-4}$. The results from the Direct Numerical Simulations differ considerably from the experimental results due to the high level of background disturbances in the oncoming flow of $Tu \approx 2\%$ in the experiment.

Further investigations are necessary and under way to investigate the influence of the turbulence level on the nature of the separation bubble.

REFERENCES

Adams, N.A., and Shariff, K., 1996, "A High-Resolution Hybrid Compact-ENO Scheme for Shock-Turbulence Interaction Problems", *Journal of Computational Physics*, Vol. 127, pp. 27-51.

Adams, N.A., 1998, "Direct Numerical Simulation of Turbulent Compression Ramp Flow", *Theoretical and Computational Fluid Dynamics*, Vol. 12, pp. 109-129.

Adams, N.A., 2001, "Direct numerical simulation of transition in compressible flows", In: *DNS/LES Progress and Challenges*, Eds.: Liu, C., Sakell, L., and Beutner, T., Greyden Press, Columbus, Ohio, pp. 171–182.

Benay, R., Chanetz, B., Mangin, B., Vandomme, L., and Perraud, J., 2006, "Shock wave/transitional boundary-layer interactions in hypersonic flow", *AIAA Journal*, Vol. 44(6), pp. 1243-1254.

Bleilebens, M., Glößer, C., Olivier, H., 2005, "High-speed Aerodynamics of the Two-Stage ELAC/EOS-Configuration for Acend an Re-entry", In: *Basic Research and Technologies for Two-Stage-to-Orbit Vehicles*, Final report of the DFG collaborative research centers 253, 255 and 259, eds.: D. Jacob, G. Sachs and S. Wagner, pp. 242-268, Wiley-VCH.

Knight,D., 2003, "RTO WG 10, Test cases for CFD validation of Hypersonic Flight", *AIAA Paper 2003-0433*, http://coewww.rutgers.edu/∼wg10/stage2.html.

Lawal, A.A., and Sandham, N.D., 2000, "Direct simulation of transonic flow over a bump", In: *Direct and Large Eddy Simulation IV*, eds.: B.J. Geurts, R. Friedrich and O. Metais, pp. 301–310, Kluwer Academic Publishing.

Loginov, M.S., Adams, N.A., and Zheltovodov, A.A., 2006, "Large-eddy simulation of shock-wave/turbulent-boundary-layer interaction", *Journal of Fluid Mechanics*, Vol. 565, pp. 135-169.

Lüdeke, H., Radespiel, R., and Schülein, E., 2004, "Simulation of streamwise vortices at the flaps of re-entry vehicles", *Aerospace Sci. Tech.*, Vol. 8, pp. 703-714.

Mack, L.M., 1969, *Boundary-Layer Stability Theory.* JPL Report 900-277 Rev. A, JPL Pasadena, USA.

Pagella, A., Rist, U., and Wagner, S., 2002, "Numerical Investigations of Small-Amplitude Disturbances in a Boundary Layer with Impinging Shock Wave at Ma=4.8", *Phys. Fluids*, Vol. 14(7), pp. 2088-2101.

Pagella, A., Babucke, A., and Rist, U., 2004, "Two-dimensional numerical investigations of small-amplitude disturbances in a boundary layer at Ma=4.8: Compression corner versus impinging shock wave", *Phys. Fluids*, Vol. 16(7), pp. 2272-2281.

Stemmer, C., and Adams, N.A., 2004, "Investigation of supersonic boundary layers by DNS" *ECCOMAS 2004 Proceedings*, Vol. II.

Stetson, K.F., Kimmel, R.L., 1992, "On Hypersonic Boundary-Layer Stability", *AIAA Paper 92-0737.*

Vandomme, L., 2004, *Contribution a l'étude de l'interaction onde de choc couche limite transitionnelle en ecoulemenent hypersonique a Mach 5* Université d'Evry Val d'Essonne, France, Ph.D. Thesis, 2004.

Wadhams T.P., and Holden, M.S., 2004, "Summary of experimental studies for cone validation in the LENS facility and comparisons with recent navier-Stokes and DSMC solutions for two- and three-dimensional separated regions in hypervelocity flows", *AIAA-paper 2004-0917.*